Supporting Information

Unravelling the pH-depended mechanism of ferroelectric polarization on different dynamic pathways of photoelectrochemical water oxidation

Xing Ji†,[a] Zhouhao Zhu†,[b] Ming Zhou,[a] Ying Zhang,[c] Liyong Gan*,[b] Yunhuai Zhang*,[a] and Peng Xiao*[b]

[a]College of Chemistry and Chemical Engineer, Chongqing University, Chongqing 401331, China.

[b]College of Physics, Chongqing University, Chongqing 401331, China.

[c]Xinjiang Key Laboratory of New Energy Materials and Green Chemical Engineering, College of Chemistry and Environmental Engineering, Xinjiang Institute of Engineering, Urumqi 830023, China

*Corresponding author: xiaopeng@cqu.edu.cn;

zyh2031@cqu.edu.cn;

ganly@cqu.edu.cn.

†Xing Ji and Zhouhao Zhu contributed equally to this work.

EXPERIMENTAL SECTION

Preparation of BTO@TiO_2 Heterojunctions. A two-step hydrothermal method was employed to successfully construct BTO@TiO_2 core-shell nanowire arrays (BTO@TiO_2 NWs), in accordance with the previously reported procedure.[1] For one thing, the TiO_2 seed layer was prepared by spin-coating on a clean FTO conductive glass using a solution containing 0.7 mL of titanium (IV) tetraisopropoxide (TTIP) and 20 μL of 37% hydrochloric acid (HCl) in 10 mL ethanol and annealed at 500 °C for one hour in air. And then, the FTO, containing TiO_2 seed layer, was placed inside a glass bottle filled with 2.5 mL 37% HCl, 2.5 mL deionized water and 45 μL TTIP. The first hydrothermal process was initiated to synthesis TiO_2 NWs at 170 °C for 4 h. After annealing at 500 °C for 1 h, TiO_2 NWs was subjected to a second hydrothermal process to construct the BTO@TiO_2 heterojunction. By reacting in a solution comprising 0.5 mmol of $Ba(OH)_2$, 0.6 g of tetrabutylammonium hydroxide, 7 mL of deionized water, 5 mL of ethanol, 5 mL of diethylene glycol and 1.5 mL of isopropanol at 150 °C for 2 h, BTO@TiO_2 NWs heterojunction was successfully synthesized. Subsequently, the products were washed with deionized water and ethanol, and dried at 60 °C for 12 h.

Morphological and Structural Characterization. X-ray diffraction (XRD, Shimadzu ZD-3AX, Cu Kα radiation) was employed to determine whether TiO_2 and BTO@TiO_2 were effectively synthesized by characterizing the crystal structure of the samples. X-ray photoelectron spectroscopy (XPS, ESCALAB 250Xi, Al Kα radiation) was utilized to identify the differences in the elemental composition of TiO_2 and BTO@TiO_2. Piezoelectric force microscopy (KPFM and SS-PFM, MFP-3D-BIO) was employed to corroborate the ferroelectric characteristics of BTO@TiO_2. The morphologies and crystalline of TiO_2 and BTO@TiO_2 NWs were determined by field-emission scanning electron microscope (FE-SEM, JEOL, JSM-7800F) and transmission electron microscope (TEM, JEM2010-HR, 200 kV). In addition, the atomic distribution of BTO surface layer was determined using atomic-scale high-angle annular dark-field characterization (HAADF, FEI Titan G2 60-300 ChemiSTEM, 300

kV).

Polarization of BTO@TiO_2 Heterojunctions. Polarization was achieved by the construction of a two-electrode system (FTO|BTO@TiO_2|FTO) with a BTO@TiO_2 photoanode and a clean FTO conductive glass in air. A voltage of 10 V was applied to the two electrodes for 10 min. This polarization treatment was considered positive when the BTO@TiO_2 photoanode was connected to the positive pole of the power source and the FTO conductive glass was connected to the negative pole. Otherwise, it was considered negative.

Photoelectrochemical Tests. Photoelectrochemical tests were carried out at the electrochemical workstation (CHI660E, Shanghai Chenhua) using a three-electrode system in which the counter electrode was platinum sheet, while the reference electrode was Ag/AgCl. A series of light-dark electrochemical scans and transient photocurrent tests were carried out across a range of pH electrolytes, including 0.5 M H_2SO_4 (pH=0), 0.5 M Na_2SO_4 (pH=7) and 1 M NaOH (pH=14). The light-dark electrochemical scans were conducted at a scan rate of 50 mV/s. The positive scans were performed under simulated solar illumination of 100 mW/cm^2 in order to ascertain the water oxidation performance of the photoanodes. The negative scans were performed in a dark environment to detect the reduction of the residual surface states. The transient photocurrents were measured at different bias voltages, with alternating light-dark intervals of 5 s and a sampling interval of 0.001 s^{-1}.

Determination of separation and catalytic efficiency. The separation (η_{sep}) and catalytic efficiency (η_{oxi}) can be expressed as follow:

$\eta_{sep} = J_{sulfite} / J_{abs}$

$\eta_{oxi} = J_{oxi} / J_{sulfite}$

where J_{oxi} is the photocurrent density for oxygen evolution under pH=2, 7 and 12. $J_{sulfite}$ is the photocurrent density for sulfite oxidation. Sulfite oxidation measures were carried out under 0.5 M Na_2SO_3 solution with pH=2, 7 and 12. J_{abs} is the theoretical maximum photocurrent of TiO_2 (1.84 mA/cm^2).

Theoretical Calculation Details. All spin-polarized density functional theory simulation was performed based on Vienna *ab initio* simulation package[2]. The exchange-correlation potentials were described by Perdew–Burke–Ernzerhof functional within generalized gradient approximation[3]. The D3 method was used to describe the effects of nonlocal van der Waals interactions[4]. The cutoff energy was set as 520 eV and Monkhorst-Pack *k*-points was set as 3×3×1 and 9×9×1 for geometry optimization and electronic structure, respectively. The convergence threshold of energy and force was set as 10^{-5} eV and 0.02 eV/Å, respectively. A z-direction vacuum layer of 20 Å was included to avoid periodic interaction.

The OER free energy change was obtained using the computational hydrogen electrode (CHE) model proposed by Nørskov *et al*.[5] which is expressed by the following equation:

$$\Delta G = \Delta E + \Delta E_{ZPE} - T\Delta S + \Delta G_{U} + \Delta G_{pH}$$

where ΔE is the total energy difference of the intermediates, ΔE_{ZPE} and $T\Delta S$ are the zero-point vibrational energy and entropy contributions at 298.15 K, respectively. ΔG_{U} and ΔG_{pH} are the free energy contribution with the applied potential U and pH, which can be defined as:

$$\Delta G_{U} = -eU$$

$$\Delta G_{pH} = -k_{B}T\ln 10 \times \mathrm{pH}$$

where k_{B} is Boltzmann constant, and the value of pH in this work is set to be 0. The charge density differences for the heterjunctions only and for *O adsorption is defined in the following

$$\rho = \rho_{TiO_2\text{-}BTO} - \rho_{TiO_2} - \rho_{BTO}$$

$$\rho_{ads} = \rho_{TiO_2\text{-}BTO@O} - \rho_{TiO_2\text{-}BTO@O} - \rho_{O}$$

where $\rho_{TiO_2\text{-}BTO@O}$, $\rho_{TiO_2\text{-}BTO}$, ρ_{TiO_2}, ρ_{BTO} and ρ_{O} are the charge density of TiO_2-BTO with *O adsorbed, TiO_2-BTO, TiO_2, BTO and an isolated O atom, respectively.

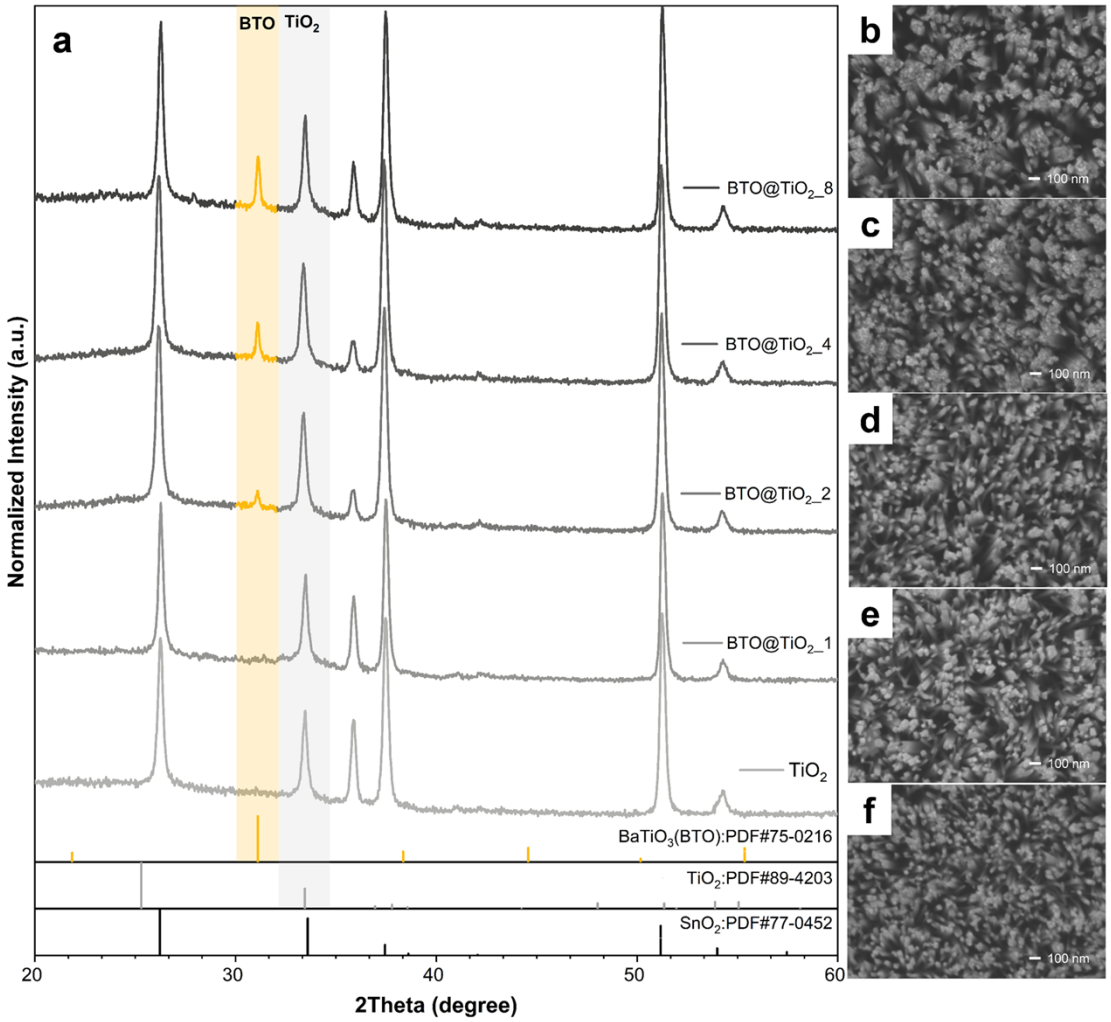

Fig. S1 (a) X-ray diffraction patterns of hydrothermally prepared TiO_2 as well as BTO@TiO_2 with different times of hydrothermal conversion. Scanning electron microscopy images of (b) TiO_2, (c) BTO@TiO_2_1 with 1 h hydrothermal reaction, (d) BTO@TiO_2_2 with 2 h hydrothermal reaction, (e) BTO@TiO_2_4 with 4 h hydrothermal reaction, and (f) BTO@TiO_2_8 with 8 h hydrothermal reaction.

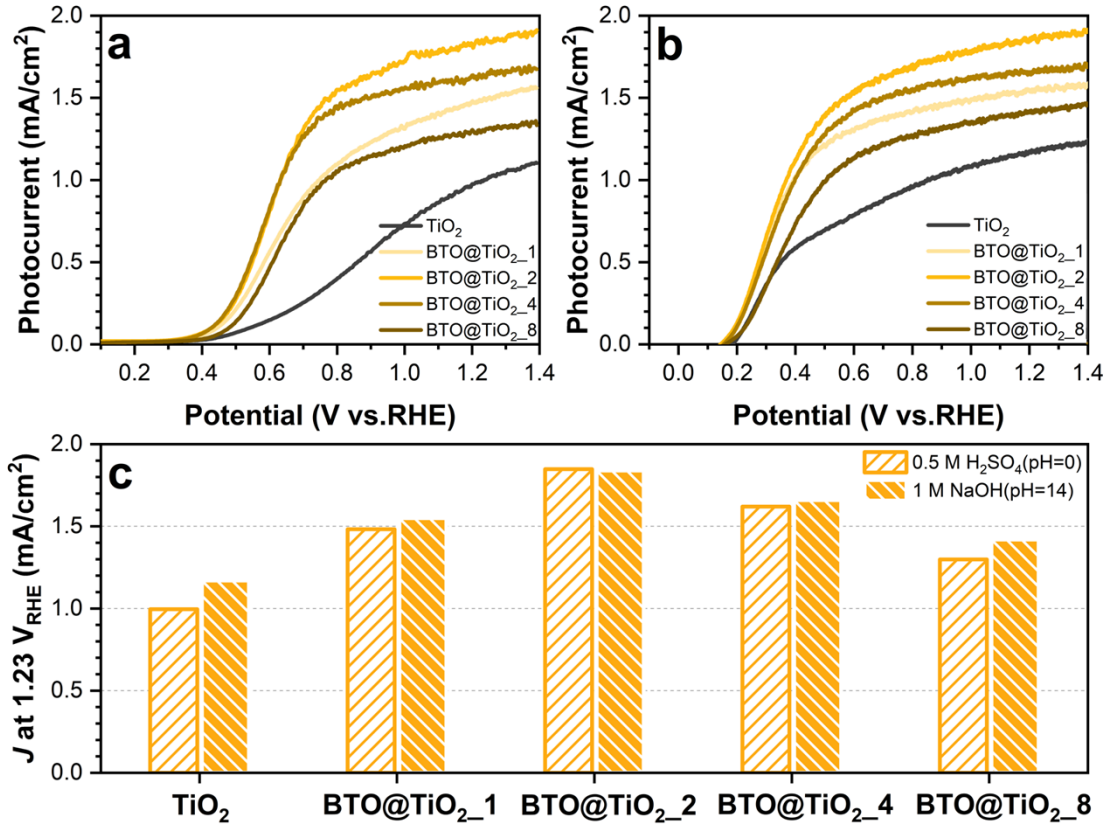

Fig. S2 The photocurrent curves of TiO_2 Nws and BTO@TiO_2 prepared with different reaction times under (a) 0.5 M H_2SO_4 (b) and 1 M NaOH electrolytes. (c) The photocurrent values of TiO_2 Nws and BTO@TiO_2 at 1.23 V_{RHE}.

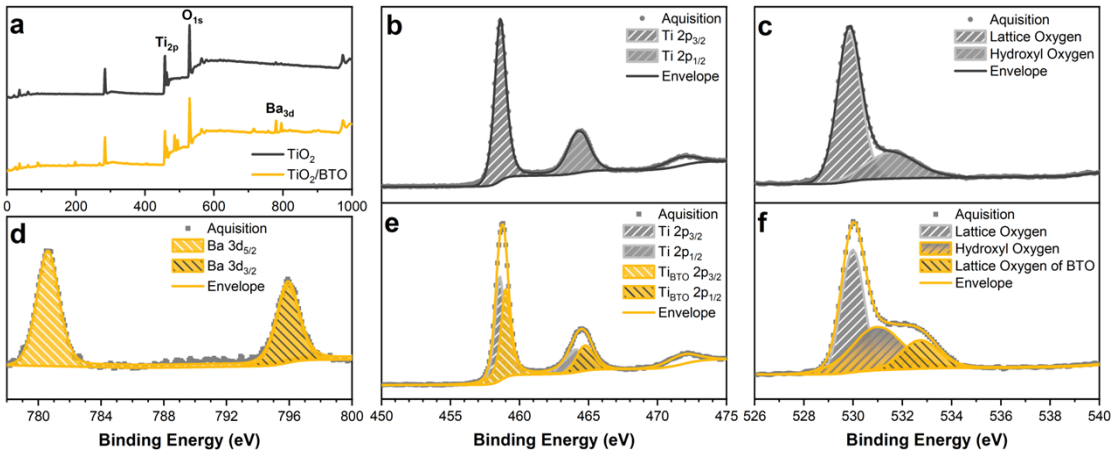

Fig. S3 (a) The photoelectron spectra of TiO_2 and BTO@TiO_2. The XPS spectra of (b) Ti 2p and (c) O 1s of TiO_2, (d) Ba 3d, (e) Ti 2p and (f) O 1s of BTO@TiO_2.

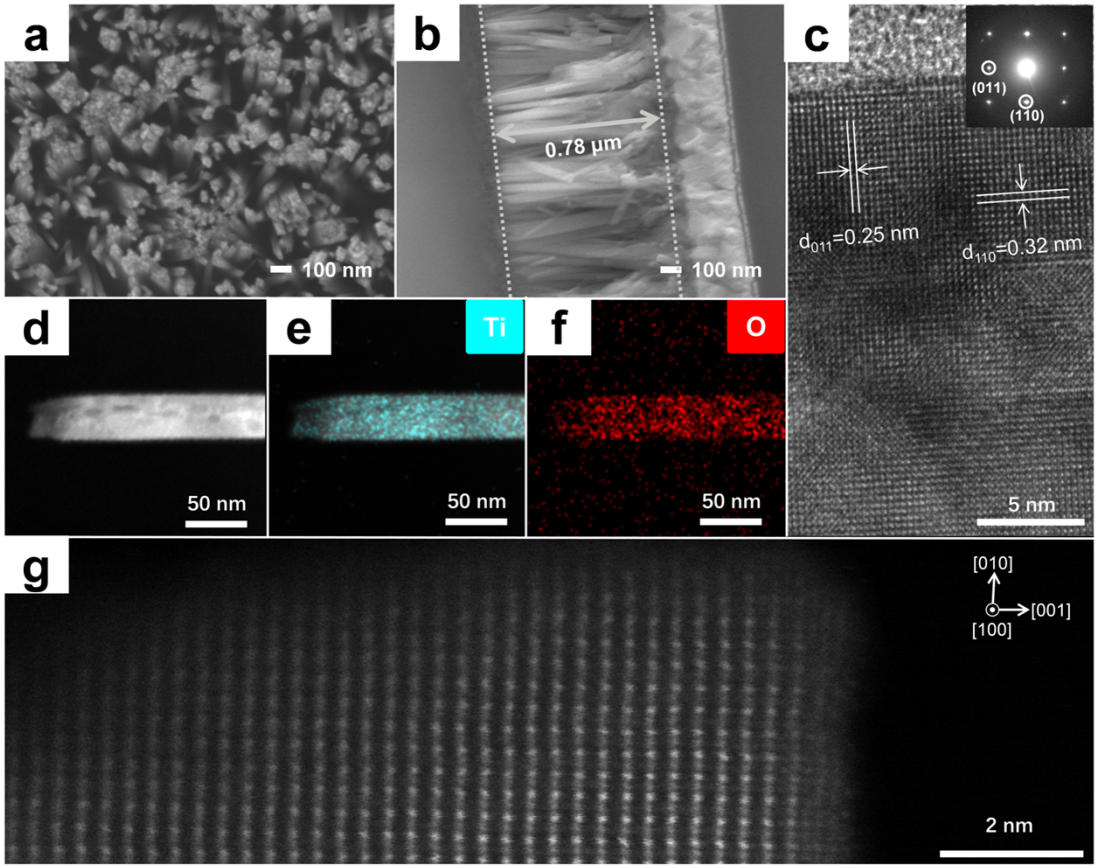

Fig. S4 SEM images of TiO_2 NWs with (a) top view and (b) side view. (c) TEM images of TiO_2 NWs. (d-f) Energy-dispersive X-ray spectroscopy (EDX) elemental distribution of TiO_2 NWs. (g) Atomic-resolution HAADF-STEM image of TiO_2 NWs.

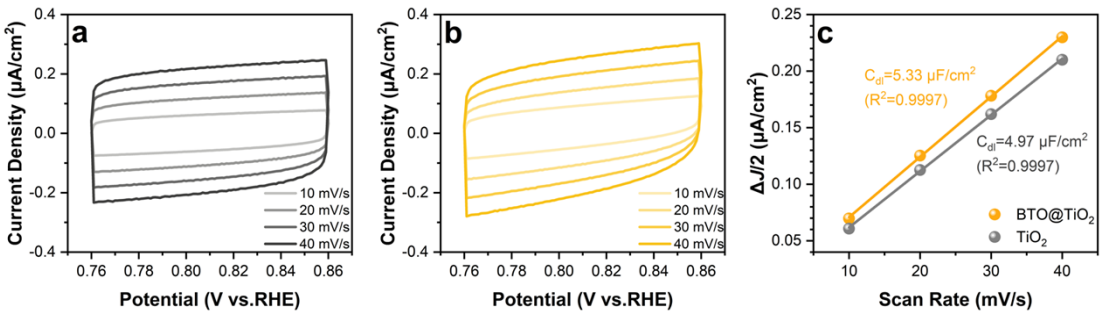

Fig. S5 Cyclic voltammetry curves of TiO_2 (a) and BTO@TiO_2 (b) at different scan rates. (c) The relationship between scan rate and $\Delta J/2$.

.

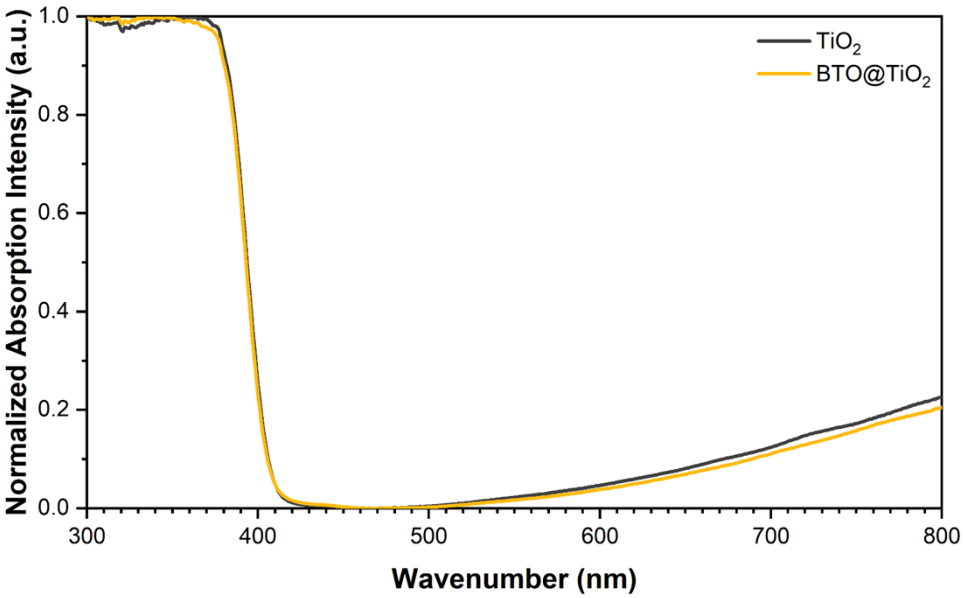

Fig. S6 The UV-visible absorption of TiO_2 and BTO@TiO_2 NWs array samples.

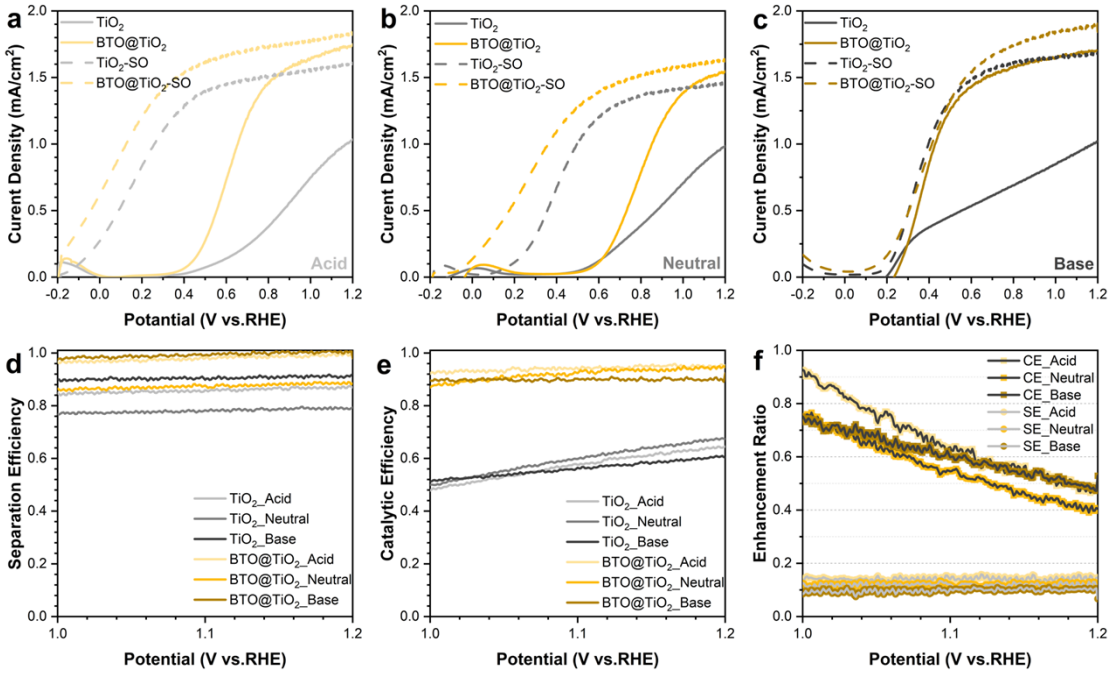

Fig. S7 The photocurrent curves of TiO_2 and BTO@TiO_2 photoanodes for oxygen evolution and sulfite oxidation with 0.5 M Na_2SO_3 in (a) acid, (b) neutral and (c) base. (d) The separation (e) and catalytic efficiency of TiO_2 and BTO@TiO_2 photoanodes under different pH electrolytes. (f) Enhancement ratio of separation and catalytic efficiency from TiO_2 to BTO@TiO_2 photoanodes under different pH electrolytes.

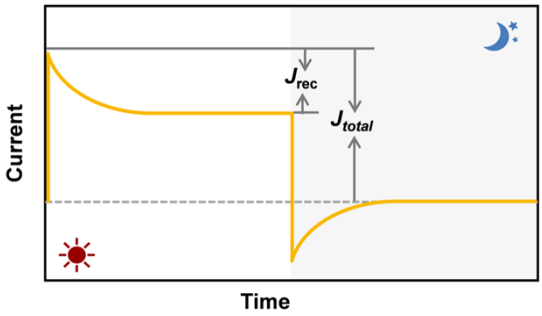

Fig. S8 An illustration on establishing the total photocurrent (J_{total}) as well as the surface recombination current (J_{rec}) through transient photocurrent response.

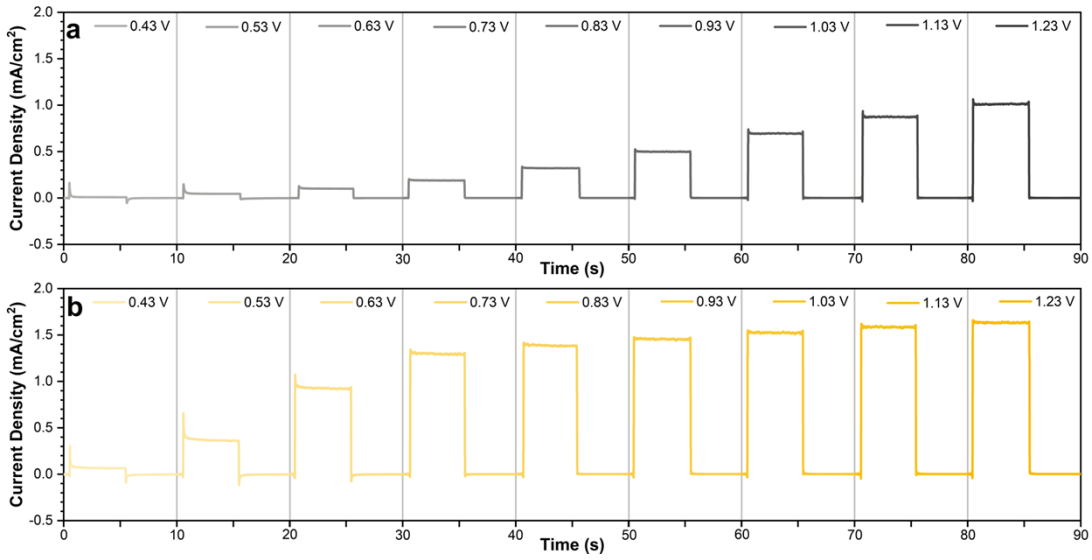

Fig. S9 Transient photocurrent spectra of (a) TiO_2 and (b) BTO@TiO_2 at different bias in 0.5 M H_2SO_4 (pH=0).

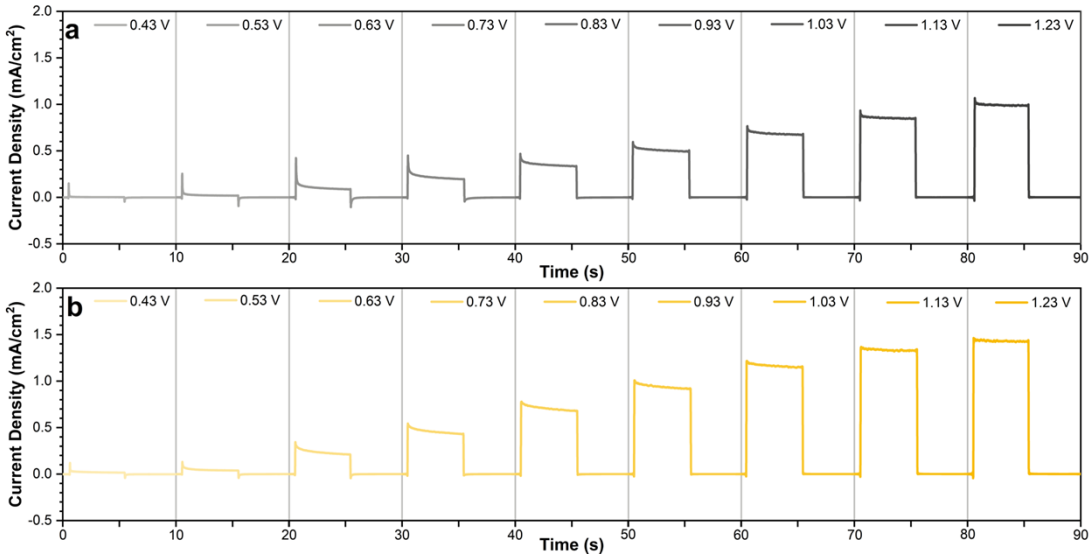

Fig. S10 Transient photocurrent spectra of (a) TiO_2 and (b) BTO@TiO_2 at different bias in 0.5 M Na_2SO_4 (pH=7).

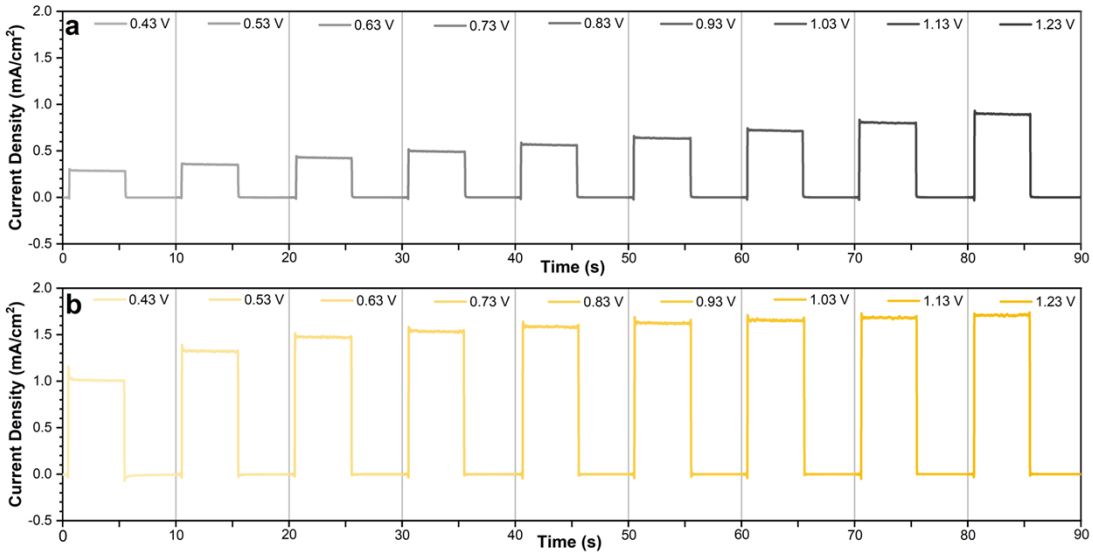

Figure S11. Transient photocurrent spectra of (a) TiO_2 and (b) BTO@TiO_2 at different bias in 1 M NaOH (pH=14).

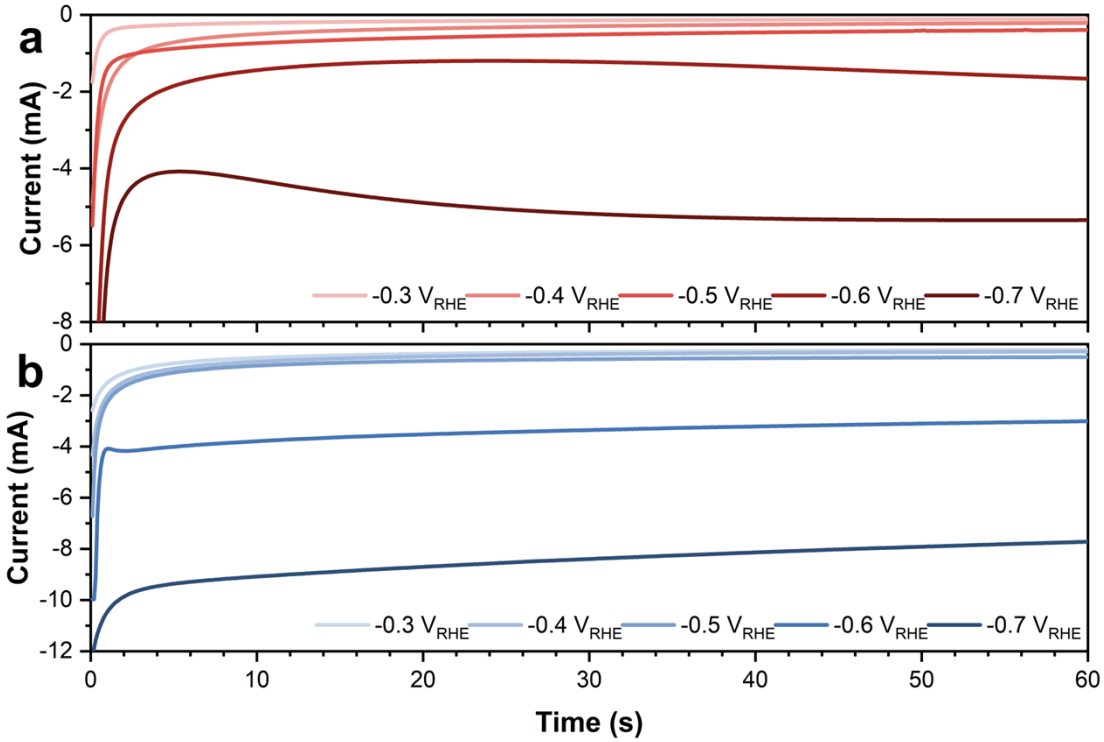

Fig. S12 The current-time curves of TiO_2 with different reduction potential in (a) 0.5 M H_2SO_4 and (b) 1 M NaOH electrolyte.

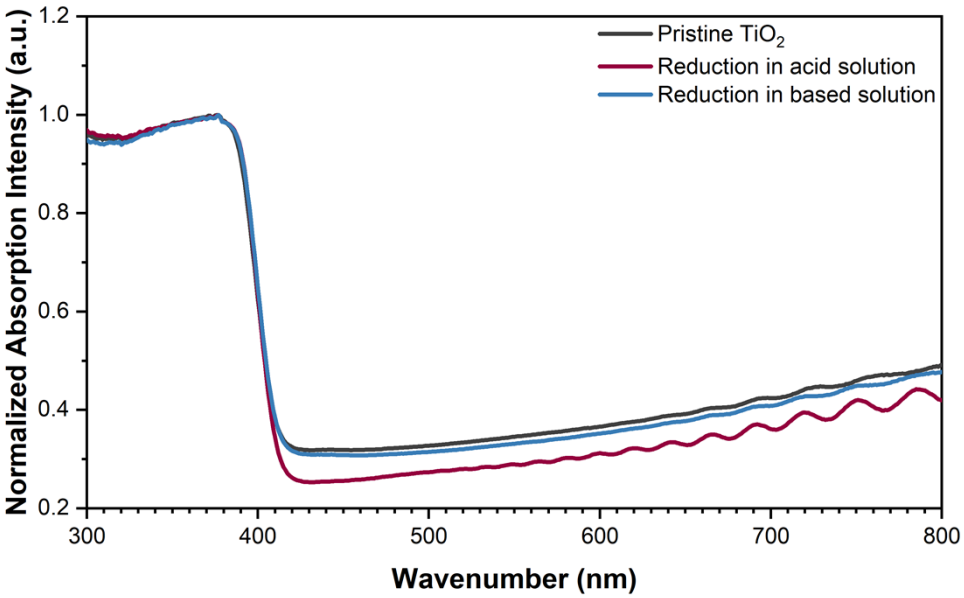

Fig. S13 The UV-visible absorption of TiO_2 before and after electrochemical reduction treatment.

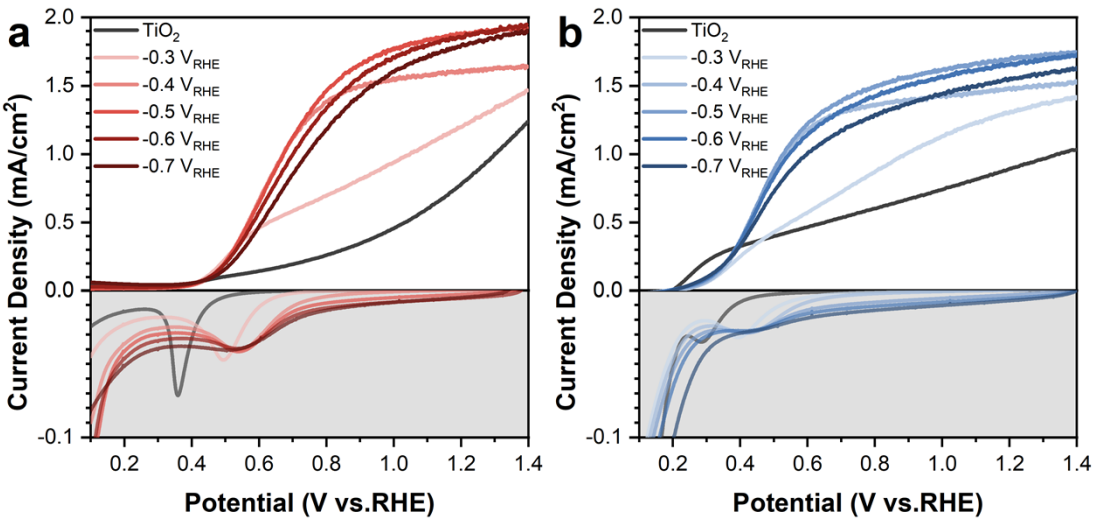

Fig. S14 Electrochemical fingerprints scan of reduced TiO_2 in (a) pH=0 and (b) pH=14.

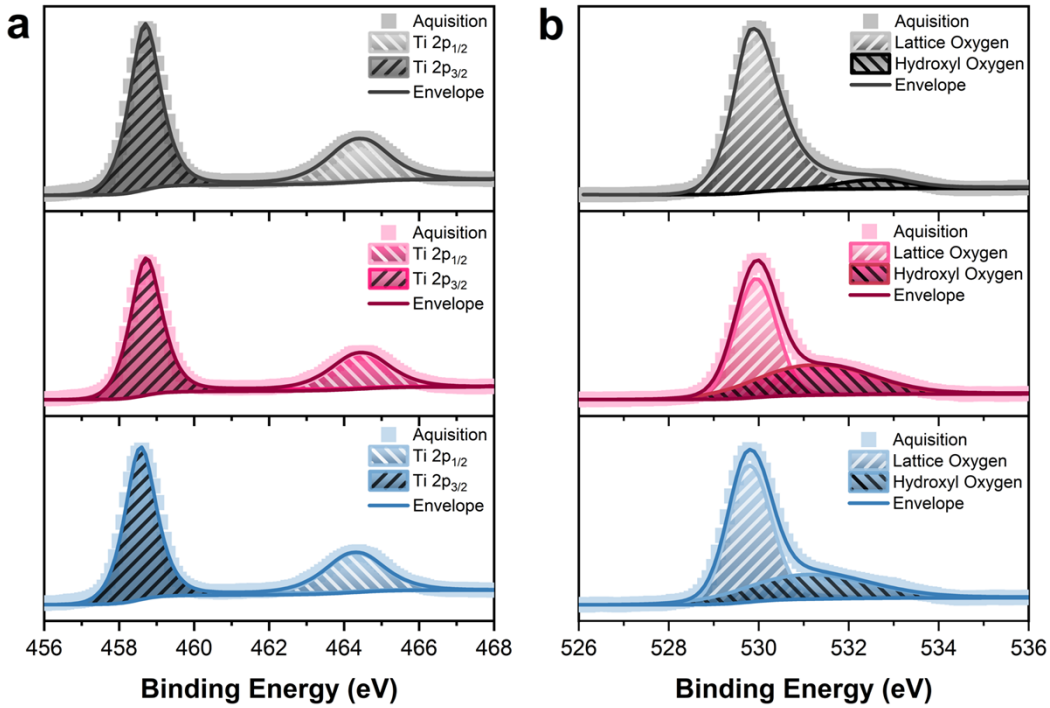

Fig. S15. XPS spectra of Ti (a) and O (b) in TiO_2 before and after electrochemical reduction.

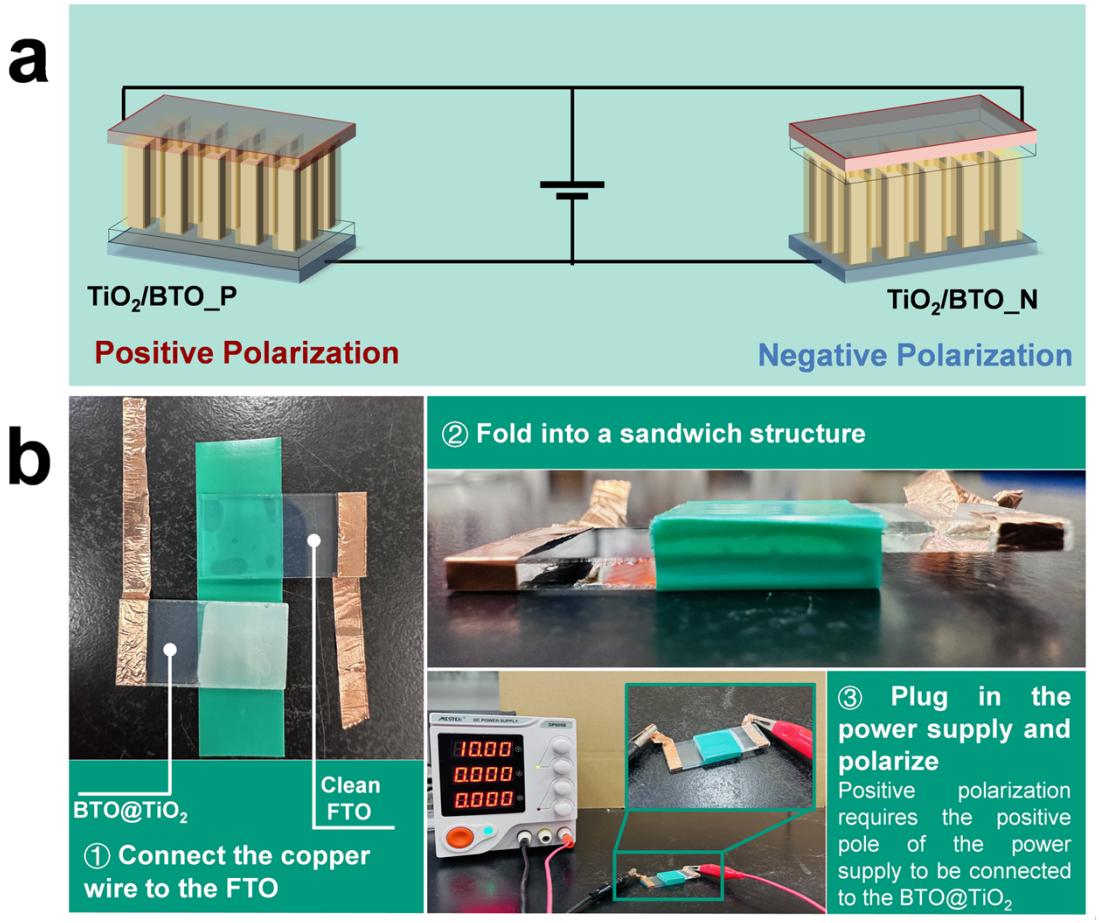

Fig. S16 (a) Diagram of the apparatus used to achieve positive and negative polarization of BTO@TiO_2. (b) The specific device to achieve polarization.

Table S1. Comparison of reported ferroelectric-based photoelectrode

Materials	Electrolyte	Poling Method	J at 1.23 V_{RHE} before poling (mA/cm^2)	J at 1.23 V_{RHE} after poling (mA/cm^2)	Polarization induced enhancement (mA/cm^2)	Reference
$BaTiO_3$	0.5 M Na_2SO_4(pH=5.95)	52.8 kV cm^{-1} in air	0.141	0.276	0.135	[6]
$BiFeO_3$	1 M KOH (pH=13.6)	+40 V in Ethanol	0.016	0.088	0.072	[7]
$BaTiO_3$-TiO_2	1 M NaOH (pH=13.6)	+3 V in 2 M KCl aqueous	1.30	1.40	0.10	[1]
$SrTiO_3$-TiO_2	1 M NaOH (pH=13.6)	+10 V in air	1.40	1.45	0.05	[8]
$BiFeO_3$/Sn: TiO_2	1 M NaOH (pH=13.6)	+2 V in 1 M KOH	1.47	1.76	0.29	[9]
$BaTiO_3$/WO_3	0.5 M PBS (pH=7)	+20 V in air	0.05	0.09	0.04	[10]
Fe_2O_3-$BaTiO_3$	1 M NaOH (pH=13.6)	+8 V in propylene carbonate	0.23	0.33	0.10	[11]
TiO_2/$BaTiO_3$/Ag_2O	1 M NaOH (pH=13.6)	+2 V in 1 M NaOH	1.30	1.55	0.25	[12]
Li-doped ZnO	0.5 M Na_2SO_4 (pH=7)	+2 V in 0.5 M Na_2SO_4	1.75	1.90	0.15	[13]
Bi_2FeCrO_6	0.5 M Na_2SO_4 (pH=7)	+15 V in air	0.10	0.15	0.05	[14]
$NaNbO_3$	0.5 M Na_2SO_4 (pH=7)	+5 V in air	0.31	0.51	0.20	[15]
Fe_2O_3/PZT	1 M NaOH (pH=13.6)	+5 V in 1 M KCl	1.00	1.25	0.25	[16]
$BaTiO_3$/Nb: $SrTiO_3$	0.1 M NaOH (pH=13)	+8 V in propylene carbonate	0.09	0.21	0.12	[17]
BTO@TiO_2	**pH=11**	**+ 10 V in air**	**1.08**	**1.60**	**0.52**	**This work**

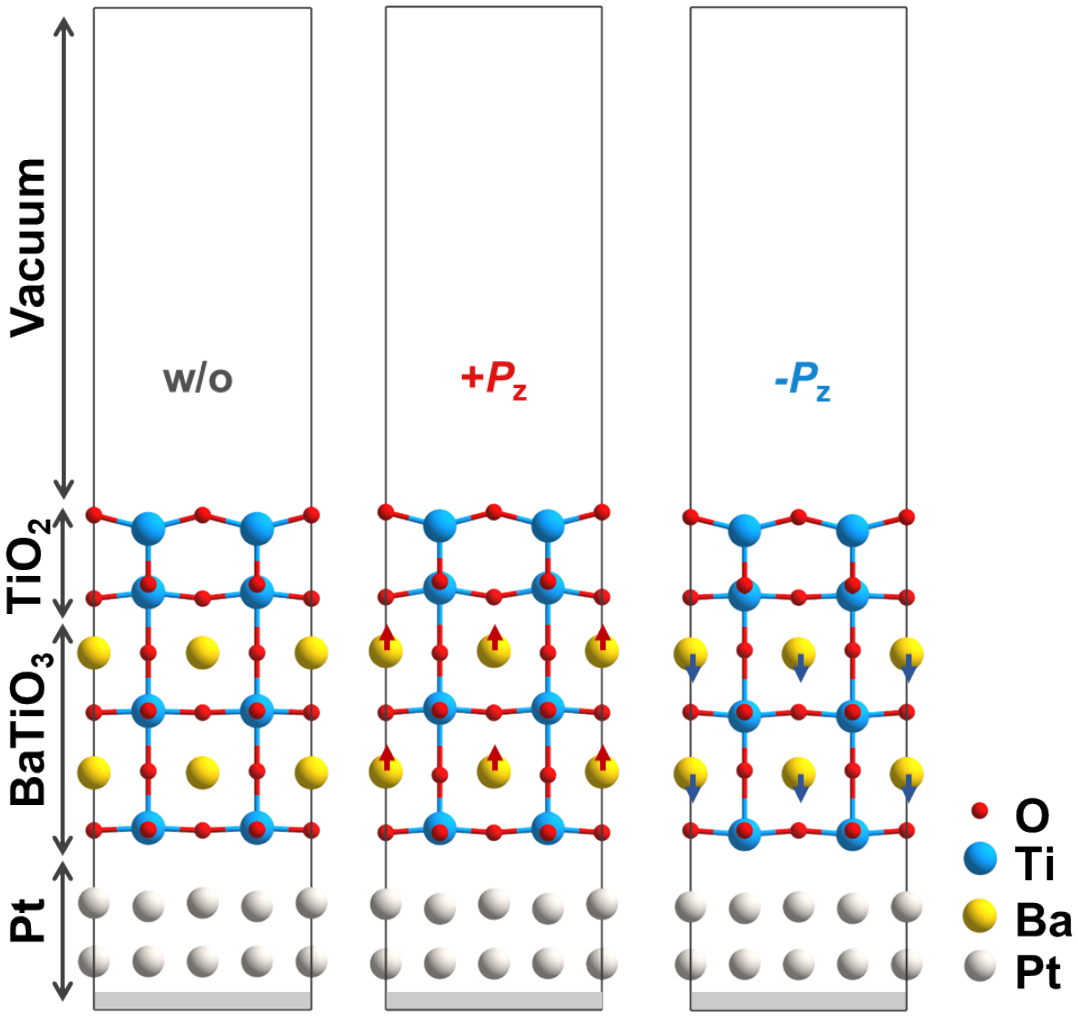

Fig. S17 The geometries of BTO@TiO_2 without (w/o) and with positive ($+P_z$) and negative polarization ($-P_z$).

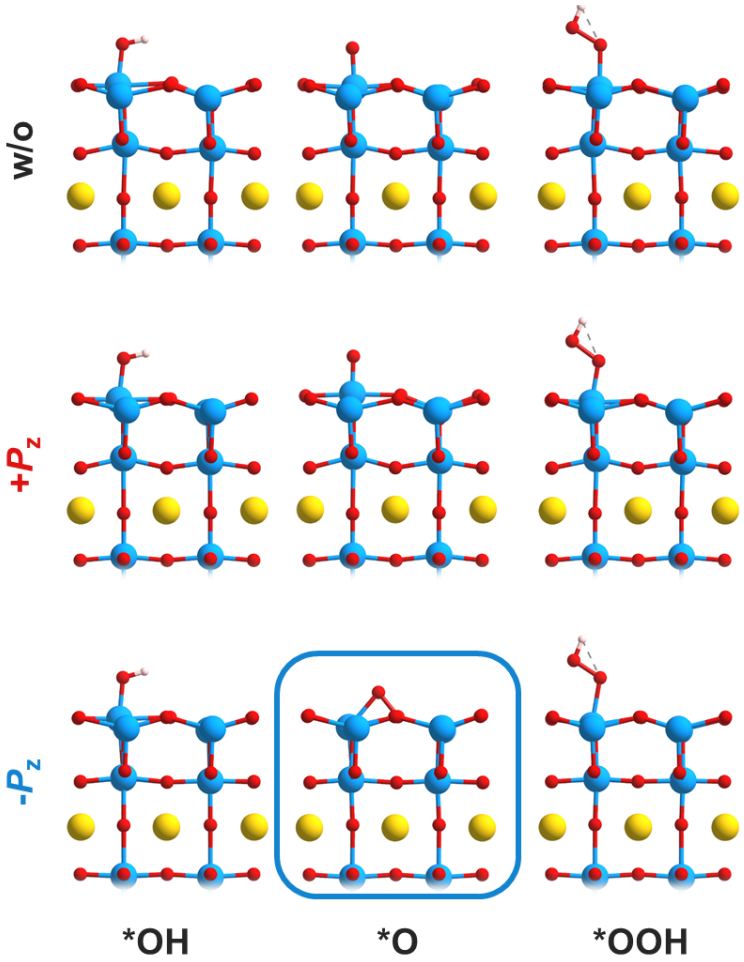

Fig. S18 Adsorption geometries of different intermediates on the w/o, $+P_z$, $-P_z$ of BTO@TiO_2

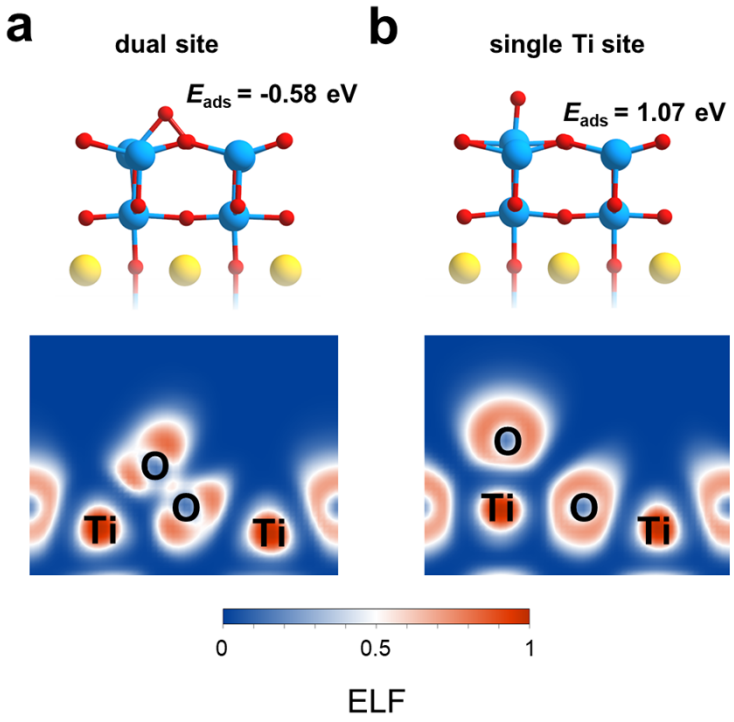

Fig. S19 Side view (upper panel) of configuration with O* adsorbed at (a) a dual site (one surface Ti and one surface O) and (b) only one surface Ti site on $-P_z$ BTO@TiO_2. Corresponding electronic localization function (ELF) plot is presented in the lower panel.

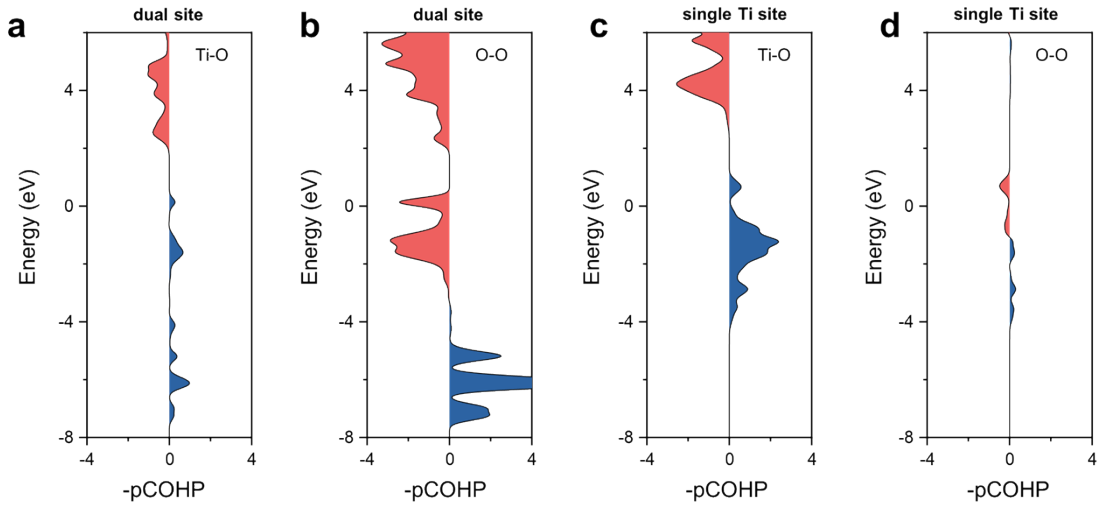

Fig. S20 Crystal Orbital Hamilton Populations (COHP) of Ti-O and O-O bond in the configuration with O* adsorbed at (a-b) a dual site and (c-d) a single Ti site on the $-P_z$ BTO@TiO_2.

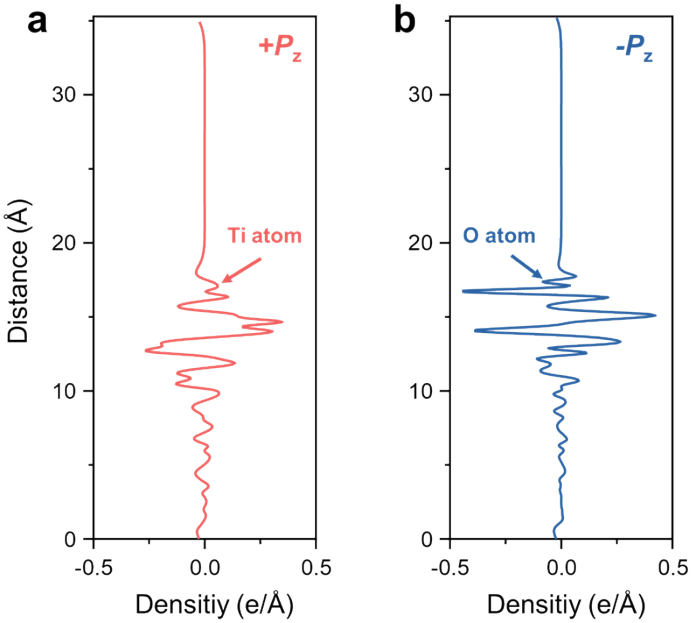

Fig. S21 Planar average charge density difference between TiO_2 and BTO in the (a) $+P_z$ and (b) $-P_z$, respectively.

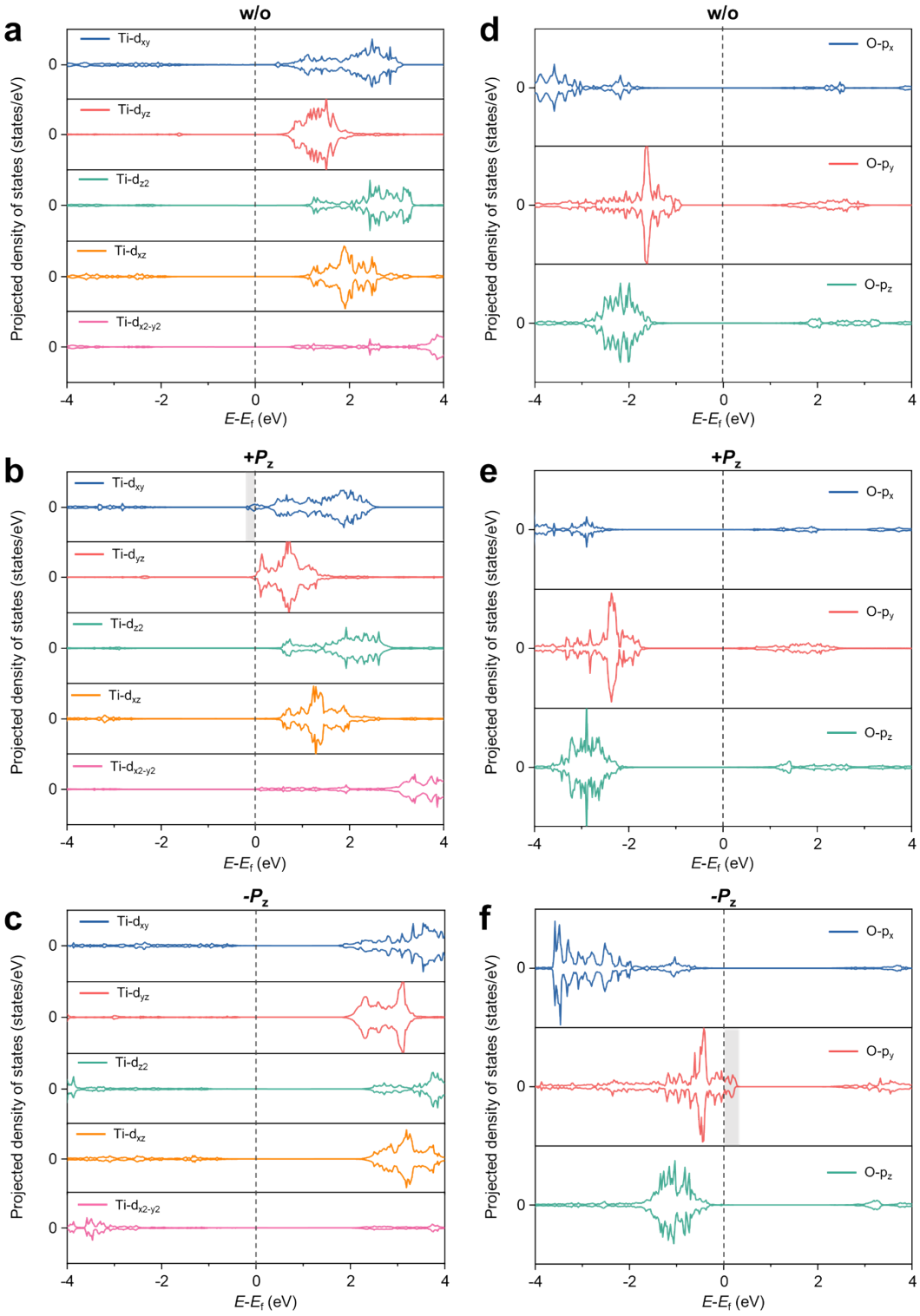

Fig. S22 Projected density of states of a surface (a-c) Ti and (d-f) O atom for the w/o, $+P_z$ and $-P_z$ BTO@TiO_2. The Fermi level (vertical dashed lines) is set to be the zero.

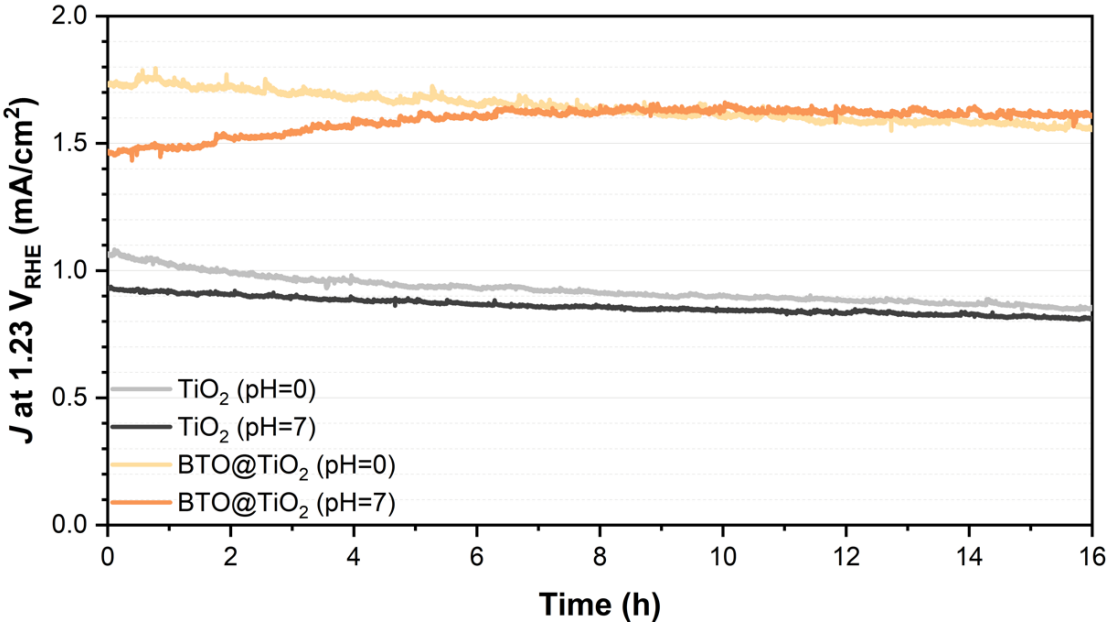

Fig. S23 The current-time curves of TiO_2 and BTO@TiO_2 obtained in acidic, neutral electrolyte under 1.23 V_{RHE}.

Reference

1. W. Yang, Y. Yu, M. B. Starr, X. Yin, Z. Li, A. Kvit, S. Wang, P. Zhao and X. Wang, *Nano Lett.*, 2015, **15**, 7574-7580.
2. G. Kresse and J. Hafner, *Phys. Rev. B*, 1993, **47**, 558-561.
3. J. P. Perdew, K. Burke and M. Ernzerhof, *Phys. Rev. Lett.*, 1996, **77**, 3865-3868.
4. S. Grimme, J. Antony, S. Ehrlich and H. Krieg, *J. Chem. Phys.*, 2010, **132**.
5. J. K. Nørskov, J. Rossmeisl, A. Logadottir, L. Lindqvist, J. R. Kitchin, T. Bligaard and H. Jónsson, *J. Phys. Chem. B*, 2004, **108**, 17886-17892.
6. S. Assavachin and F. E. Osterloh, *J. Am. Chem. Soc.*, 2023, **145**, 18825-18833.
7. X. Li, Z. Wang, W. Ji, T. Lu, J. You, K. Wang, G. Liu, Y. Liu and L. Wang, *ACS Nano*, 2023, **17**, 22944-22951.
8. F. Wu, Y. Yu, H. Yang, L. N. German, Z. Li, J. Chen, W. Yang, L. Huang, W. Shi, L. Wang and X. Wang, *Adv. Mater.*, 2017, **29**, 1701432.
9. J. Huang, Y. Wang, X. Liu, Y. Li, X. Hu, B. He, Z. Shu, Z. Li and Y. Zhao, *Nano Energy*, 2019, **59**, 33-40.
10. Y. Zhu, X. Ji, Y. Xiong, J. Guo, S. Yao, Q. Lai, P. Li, Y. Zhang and P. Xiao, *Mater. Sci. Semicond. Proces.* 2021, **133**, 105958.
11. M. Sima, E. Vasile, N. Preda, A. Sima, E. Matei and C. Logofatu, *Int. J. Hydro. Energy*, 2021, **46**, 36232-36244.
12. Z. Liu, L. Wang, X. Yu, J. Zhang, R. Yang, X. Zhang, Y. Ji, M. Wu, L. Deng, L. Li and Z. L. Wang, *Adv. Funct. Mater.*, 2019, **29**, 1807279.
13. H. J. Lee, S.-H. Shin, K. T. Nam, J. Nah and M. H. Lee, *J. Mater. Chem. A*, 2016, **4**, 3223-3227.
14. W. Huang, C. Harnagea, X. Tong, D. Benetti, S. Sun, M. Chaker, F. Rosei and R. Nechache, *ACS Appl. Mater. Inter.*, 2019, **11**, 13185-13193.
15. S. Singh and N. Khare, *Appl. Phys. Lett.*, 2017, **110**.
16. X. He, B. Lin, L. Yang, C. Shang, S. Li, Z. Chen and X. Wang, *Energy & Fuels*, 2020, **34**, 16927-16935.
17. M. Rioult, S. Datta, D. Stanescu, S. Stanescu, R. Belkhou, F. Maccherozzi, H. Magnan and A. Barbier, *Appl. Phys. Lett.*, 2015, **107**.